Author/s:
Yan, W;Johnson, BC;Balendhran, S;Cadusch, J;Yan, D;Michel, JI;Wang, S;Zheng, T;Crozier, K;Bullock, J

Title:
Visible to Short-Wave Infrared Photodetectors Based on ZrGeTe4van der Waals Materials

Date:
2021-09-29

Citation:
Yan, W., Johnson, B. C., Balendhran, S., Cadusch, J., Yan, D., Michel, J. I., Wang, S., Zheng, T., Crozier, K. & Bullock, J. (2021). Visible to Short-Wave Infrared Photodetectors Based on ZrGeTe4van der Waals Materials. ACS Applied Materials and Interfaces, 13 (38), pp.45881-45889. https://doi.org/10.1021/acsami.1c12564.

Persistent Link:
https://hdl.handle.net/11343/295016

# Visible to Short-Wave Infrared Photodetectors Based on $ZrGeTe_4$ van der Waals Materials

*Wei Yan[1,#], Brett C. Johnson[2,3,#], Sivacarendran Balendhran[2], Jasper Cadusch[1], Di Yan[1], Jesús Ibarra Michel[1],Shifan Wang[1], Tian Zheng[4], Kenneth Crozier[1,2,5], James Bullock[1,*]*

[1]Department of Electrical and Electronic Engineering, University of Melbourne, Victoria 3010, Australia. [2]School of Physics, University of Melbourne, Victoria 3010, Australia.
[3]School of Engineering, RMIT University, Victoria 3001, Australia.
[4]Materials Characterisation and Fabrication Platform (MCFP), Department of Chemical Engineering, University of Melbourne, Victoria 3010, Australia. [5]Australian Research Council (ARC) Centre of Excellence for Transformative Meta-Optical Systems (TMOS), University of Melbourne, Victoria 3010, Australia.

[#]Wei Yan and Brett C. Johnson have contributed equally to this article.
[*]Corresponding Author: james.bullock@unimelb.edu.au

**Key words**

van der Waals materials, infrared photodetector, $ZrGeTe_4$, visible, short-wave infrared, van der Waals materials stability.

## Abstract

The self-terminated, layered structure of van der Waals materials introduces fundamental advantages for infrared (IR) optoelectronic devices. These are mainly associated with the potential for low noise whilst maintaining high internal quantum efficiency when reducing IR absorber thicknesses. In this study, we introduce a new van der Waals material candidate, Zirconium Germanium Telluride ($ZrGeTe_4$), to a growing family of promising IR van der Waals materials. We find the bulk form $ZrGeTe_4$ has an indirect band edge around ~0.5 eV, in close agreement with previous theoretical predictions. This material is found to be stable up to 140 °C and shows minimal compositional variation even after >30 days storage in humid air. We demonstrate simple proof-of-concept broad spectrum photodetectors with responsivities above 0.1 A $W^{-1}$ across both the visible and short-wave infrared wavelengths. This corresponds to a specific detectivity of ~$10^9$ cm $Hz^{1/2}$ $W^{-1}$ at $\lambda = 1.4$ μm at room temperature. These devices show a linear photoresponse vs. illumination intensity relationship over ~4 orders of magnitude, and fast rise/fall times of ~50 ns, also verified by a 3dB roll-off frequency of 5.9 MHz. As the first demonstration of photodetection using $ZrGeTe_4$, these characteristics measured on a simple proof-of-concept device, shows the exciting potential of $ZrGeTe_4$ for room temperature IR optoelectronic applications.

## Introduction

Optoelectronic devices that collect or emit photons in the short-wave infrared (SWIR, 1.4-3 μm) band are used in fields such as imaging, thermophotovoltaics and optical communication.[1-11] Presently these application spaces are dominated by materials such as $In_xGa_{1-x}As$ and $Hg_{1-x}Cd_xTe$,[12, 13] which have been engineered over decades to provide near unity quantum efficiencies.[14, 15] Despite the maturity of these technologies there are still fundamental roadblocks intrinsically associated with the use of three-dimensional (3D) semiconductors, for example volume dependent thermal noise.[16, 17] In SWIR photodetectors, these limitations impose tradeoffs between sensitivity and cost or size. As such, there is significant interest in the exploration of alternative materials with the potential to overcome such limitations.

Recently, a suite of two-dimensional (2D) van der Waals materials with bandgaps in the short-, mid- and long-wave IR regions have demonstrated surprisingly high figures-of-merit for photodetection, including graphene,[1, 18] black phosphorus,[19-23] black phosphorus arsenic,[24] platinum diselenide,[25-28] palladium diselenide,[29] molybdenum telluride,[30] niobium sulfide,[31] and tellurium.[32] In the context of photodetection, the primary advantages of these materials stem from their naturally self-terminated, layered structure. This allows extreme thickness scaling, in some cases down to the nm-scale, without excessive surface recombination. This allows both low volume-dependent thermal noise and high internal quantum efficiency. However, extreme thickness scaling must be balanced against lower absorption in thinner layers and some studies have found that moderately thick layers (i.e. 20-300 nm) represent a good compromise between low noise and high absorption.[21, 24, 33] The 2D surfaces also allow the formation of functional van der Waals interfaces/heterojunctions without having to consider lattice matching, as is the case for high quality III-V materials. .[34-42]

Prompted by the $>10^{10}$ cm $Hz^{1/2}$ $W^{-1}$ room temperature detectivities already demonstrated in the MWIR region using bP, the hunt for new IR van der Waals materials has grown with a particular emphasis on finding materials with greater stability against light, moisture, oxygen and temperature. The ternary van der Waals material $ZrGeTe_4$ is one potential candidate, which up to now has remained unexplored for optoelectronic applications. $ZrGeTe_4$ is predicted to have a narrow indirect band gap (0.2-0.7 eV) in its bulk form and a wider direct gap (1.08-1.2 eV) in its monolayer form, and exhibits in-plane anisotropy. As shown in **Figure 1a**, it has an orthorhombic crystal structure with lattice constants of $a = 3.98$ Å, $b = 10.95$ Å, $c = 15.88$ Å and angles $\alpha = \beta = \gamma = 90^o$.[43] This study investigates the stability and photodetection capabilities of bulk $ZrGeTe_4$ as a new member of the family of IR van der Waals material absorbers. Using a relatively simple detector structure, photodetector results approaching those of more mature material systems are obtained.

The $ZrGeTe_4$ absorbers trialed in this work are mechanically exfoliated from high quality bulk crystals grown by the flux method (*2Dsemiconductor.com*). **Figure 1b** shows the X-ray diffraction (XRD) spectrum of bulk $ZrGeTe_4$ flakes exfoliated onto a $Si/SiO_2$ carrier substrate. Spectra from the $Si/SiO_2$ substrate without $ZrGeTe_4$ is shown for comparison. The diffraction peaks appear at 11.1°, 22.3°, 33.5°, 45.3°, and 57.6°, which are indexed to the (020), (040), (060), (080) and $(0\underline{10}0)$ planes of $ZrGeTe_4$, respectively. These peak positions agree well with previous reports of $ZrGeTe_4$.[43] A Raman spectrum is presented in **Figure 1c** showing six characteristic Raman peaks appearing at 102.5, 117.1, 174.3, 185.9, 219.0 and 240.8 $cm^{-1}$ as determined with Lorentzian fits to the room temperature data (fit details provided in supplementary material **Table S1** and **Figure S1**). Again, these values agree well with previous measurements on $ZrGeTe_4$.[43]

Thermal stability and material interactions with oxygen, humidity and light are important considerations when assessing if a new candidate is suitable for IR detection. To investigate the stability of $ZrGeTe_4$, we monitor the Raman spectra of samples whilst subjecting them to the above stressors. **Figure 2a** shows the change in the Raman spectrum as a function of the 532 nm laser excitation power as indicated. The exposure time was 100 seconds and the laser spot size was ~0.9 μm in diameter. Clear modifications in the Raman spectrum associated with decomposition of the $ZrGeTe_4$ structure can be observed for laser power densities above 2 $mW/\mu m^2$. Possible decomposition products include amorphous ZrTe and amorphous GeTe.[44, 45] A clear indicator of phase transformation is the appearance of a peak around 140 cm$^{-1}$, which is distinct from the $ZrGeTe_4$ as-exfoliated spectra. Similarly, **Figure 2b** shows spectra taken in-situ while the sample temperature was increased from room temperature up to 410 ºC at increments of 10 ºC, in a dry nitrogen ambient. Only selected spectra are shown in **Figure 2b** for clarity with the complete data set provided in the **Figure S2** of supplementary material. Aside from the reversible temperature dependent changes, such as the phonon mode shifts and broadening,[43] the appearance of the 140 cm$^{-1}$ peak at ~140 ºC marks the beginning of permanent structural changes in the crystal. The top spectrum was collected from a sample measured at 40 ºC after cooling from 410 ºC. This represents the spectrum of a completely transformed sample. These observations are further supported by XRD measurements taken on $ZrGeTe_4$ flakes as a function of annealing temperature shown in **Figure 2c**. The characteristic $ZrGeTe_4$ peaks show signs of transformation by 200 ºC, and completely disappear beyond the resolution of the measurement by 400ºC. The transformation of $ZrGeTe_4$ can be clearly seen by visual inspection. Optical micrographs of a $ZrGeTe_4$ flake as a function of temperature are provided in supplementary Figure S3, in which clear optical changes are evident by 200 ºC. Finally, **Figure 2d** shows Raman spectra measured on the same flake before and after 33 days of exposure to ambient conditions (air, ~20 ºC, 30-60% Relative Humidity), with a control flake measured after an identical period stored in a low $O_2$/$H_2O$ nitrogen box. Again, the appearance of the 140 cm$^{-1}$ peak indicates that decomposition has occurred but only for the sample exposed to air. This peak is absent from the samples stored in $N_2$ indicating greater stability in this environment. It should also be noted that evidence of structural instability at the edges of the flake was found even in the as-exfoliated form, with the appearance of the same Raman peak at 140 cm$^{-1}$, as shown in supplementary material **Figure S4**. Thus, we have determined $ZrGeTe_4$ is ideally fabricated without prolonged exposure to temperatures >140 ºC, whilst avoiding visible illumination at power densities significantly greater than 2 mW/μm$^2$ and lengthy air exposure times. Further details of the $ZrGeTe_4$ Raman spectra before and after transformation upon annealing at 410 °C are provided in supplementary material **Table S1** and **Figure S1**.

Next, to investigate the potential of $ZrGeTe_4$ in optoelectronic applications, proof-of-concept SWIR photodetectors are fabricated. **Figure 3a** shows an optical micrograph of a $ZrGeTe_4$ device, fabricated by mechanical exfoliation and transfer onto a Si/$SiO_2$ (285 nm) chip. For these devices, we utilize bulk $ZrGeTe_4$ flakes with thicknesses 100-340 nm, which likely have resonances in the SWIR region and hence show enhanced absorption. The Cr/Au (10/100 nm) metal electrodes were defined by electron-beam lithography (EBL) and deposited by electron-beam evaporation. These electrodes form Schottky barriers with $ZrGeTe_4$ as seen in the dark source-drain current-voltage $I_{SD}$-$V_{SD}$ curve shown in **Figure 3b**. The "S-shaped" non-Ohmic behavior is typical of a device with two opposing Schottky barriers.[46, 47] Preliminary studies revealed the ability to engineer the Schottky barrier height using low/high work function electrodes (see **Figure S5**), but Cr/Au contacts were favored in this initial study due to their consistently higher performance. The >100 nm thickness of the $ZrGeTe_4$ flakes used in this study allowed only very weak back gate control over the channel resistivity, and as such, all characterization is performed at $V_G = 0$ V. Example gate dependent drain current curves $I_{SD}(V_G)$ are provided in supplementary material **Figure S5b** and suggest that the $ZrGeTe_4$ flakes used in this study were p-type.

**Figure 3c** shows the measured spectral responsivity $R(\lambda)$ of a representative $ZrGeTe_4$ photodetector, measured at a fixed source-drain bias of $V_{SD} = 1$ V, from visible to infrared wavelengths. The visible portion of this spectrum was measured using a calibrated visible quantum efficiency analyzer, while the SWIR portion was measured using a photodetector characterization setup attached to the external port of a Fourier transform infrared (FTIR) spectrometer. The data point shown by the pink dot was obtained using a 2.2 μm laser, which agrees with the measurements made using the FTIR. In all cases the responsivity was measured by calibrating the respective setups with a commercial calibrated photodetector, more details on the measurement setup and conditions can be found in the Methods section. All three sources show a reasonable level of agreement in terms of the obtained $R(\lambda)$. A strong photoresponse is seen up to ~1.6 μm, consistent with the predicted direct gap of ~0.75 eV, whilst a weaker photoresponse extends beyond ~2.2 μm, in reasonable alignment with the predicted ~0.6 eV indirect gap.[48] The left and right panels of **Figure 3d** further investigate the bulk band edge of $ZrGeTe_4$. The left plot shows photoresponse from three representative $ZrGeTe_4$ devices extending to ~0.5 eV while the right shows a Tauc plot, extracted using transmission/reflection measurements, which suggests a band edge slightly < 0.6 eV. We note that this Tauc extraction is subject to error due to both difficulties of measuring transmission/reflection on small flakes and error induced by $H_2O$ (~5300 $cm^{-1}$) and $CO_2$ (3500-4000 $cm^{-1}$) atmospheric absorption near the extraction point.[49] It should also be noted, in this study thicker $ZrGeTe_4$ flakes generally yielded higher performance, likely owing to greater absorption. This can be partially seen in **Figure 3d**, and more explicitly in supplementary material **Figure S7d**. Significant effort was devoted towards the fabrication and testing of thinner (<100 nm) $ZrGeTe_4$

devices to extend this thickness range. However, the strong interlayer coupling of $ZrGeTe_4$ greatly reduced the yield of thin layer flakes via mechanical exfoliation, particularly in the few-layer regime. We were unable to produce devices from thin $ZrGeTe_4$ flakes with a response above the measurement resolution of the FTIR setup.

Supporting the above Raman results, it was found that the spectral responsivity of devices does not change over 2.5 months when stored in $N_2$ (see supplementary material **Figure S7a)**, but we did notice a gradual decay in performance when subjected to high power illumination in air. As expected from the thickness of the absorber, application of a gate bias was found to have negligible effect on the photoresponse (see **Figure S7b)**.

Several other tests were conducted on the influence of source-drain bias and illumination source polarization. **Figure 3e** shows the source-drain bias dependent spectral photoresponse of a representative $ZrGeTe_4$ device. The presented photoresponse map was linearly interpolated from data obtained at $V_{SD}$ = -1.5V, -1 V, -0.5 V, -0.1 V, 0 V, 0.1 V, 0.5 V, 1.0 V, and 1.5 V biases. All points were normalized to the peak photoresponse of the series, which was measured at $V_{SD}$ = -1.5 V. The photoresponse was largely symmetrical with only a very small photoresponse at $V_{SD}$ = 0 V. Example spectra used in the construction of this map are included in **Figure S6**. The $ZrGeTe_4$ photodetectors also exhibited polarization angle dependence as expected from the in-plane crystal anisotropy of this material. As shown in supplementary material **Figure S6b**, the device shows a slight linear polarization dependence around 1.8 µm, which is significantly less pronounced than behavior previously reported for Te and bP based photodetectors.[21, 32, 50]

To directly compare the signal-to-noise performance of the proof-of-concept $ZrGeTe_4$ detector to other photodetectors, its specific detectivity ($D^*$) was calculated. This is defined as follows:[51, 52]

$$D^* = \frac{R\sqrt{A\Delta f}}{i_n} \qquad (1)$$

where $A$ is the detector area, $R$ is the responsivity (such as that shown in **Figure 3c**), $\Delta f$ is the bandwidth, and $i_n$ is the noise current.[53, 54] In the ideal case, the $i_n$ would be dominated by the shot noise from the dark current which can be estimated from the equation $\overline{i_n^2} = 2eI_{dark}\Delta f$.[32, 55] In reality, other noise mechanisms contribute at low modulation frequencies as seen in supplementary material **Figure S7c**, which shows the directly measured noise spectral density of a representative $ZrGeTe_4$ device (plus instrumentation) taken under $V_{SD}$ = 1 V bias. However, at modulation frequencies beyond the corner frequency $f_c$ ~30 kHz, the above shot noise estimation is in reasonable agreement with the direct measurement. Using this estimation, the $D^*$ of a representative photodetector is calculated at λ = 1.4 and 2.0 μm as a function of bias and provided in **Figure 3f**. A peak $D^*$ value of ~$10^9$ cm $\mathrm{Hz}^{1/2}$ $\mathrm{W}^{-1}$ at λ = 1.4 μm is obtained for the $ZrGeTe_4$ photodetector when biased above $V_{SD}$ = 500 mV. This number is remarkably high given the primitive design of the detector. We anticipate that by optimizing the device architecture to increase light absorption and decrease noise, the detectivity can be improved.

Other important photodetector performance metrics are linearity and frequency response. These parameters were measured on $ZrGeTe_4$ detectors, with the results summarized in **Figure 4**. **Figure 4a** shows the measured current through a representative $ZrGeTe_4$ device when subjected to mechanically chopped variable power λ = 2.2 μm illumination under $V_{SD}$ = 1V. This data and a similar set measured under $V_{SD}$ = 0 V, were used to construct the linearity plots shown in **Figure 4b.** Two consistent linear trends between the optical power density and photocurrent density $J$ under $V_{SD}$ = 0 V and 1 V bias are seen. We note that this illumination source has a wavelength close to the band edge of $ZrGeTe_4$. It exhibits a linear input/output relationship over a broad dynamic range—at least 4 orders of magnitude. As shown in **Figure 4c**, there is also no observable baseline drift when measuring photoresponse at a fixed incident intensity (λ = 2.2 μm, 200 Hz).

Next, the maximum speed of the $ZrGeTe_4$ detector was explored by subjecting it to high frequency electrically modulated IR illumination (λ = 1.55 μm, 400 kHz-10 MHz). An example of a representative detector's response under $V_{SD}$ = 1 V is shown in **Figure 4c** for a modulation frequency ~990 kHz. Note that to ensure that instrumentation did not obscure the observable frequency response of the $ZrGeTe_4$ detector, a low gain (high bandwidth) setting was used during the pre-amplification stage, which explains the lower and noisier signal. The rise and fall times, shown in **Figure 4d**, measured at 1 V bias, are found to be ~53 ns and ~54 ns, respectively. The dashed pink lines show the square wave electrical signal used to drive the λ = 1.55 μm illumination source. To further confirm this response speed, the 3dB roll-off frequency was measured by subjecting the same $ZrGeTe_4$ detector, biased at $V_{SD}$ = 1 V, to a sinusoidally modulated illumination source (λ=1.55 μm) across the 400 kHz-10 MHz frequency range. **Figure 4e** shows the measured change in peak-to-trough response with a 3dB point at ~5.9 MHz, aligning well with the above measured response times according to the commonly used relationship $\tau_r=0.35/f_{3dB}=59.3$ ns. Characterization using a more intense, pulsed illumination source (λ=2.3 μm, pulse width ~2 ns) suggested response speeds of a similar magnitude, as shown **Figure S8**.

Finally, we perform laser beam induced current (LBIC) mapping to further investigate the operation principle of the $ZrGeTe_4$ device (**Figure 5**). The LBIC system is based on a custom-built confocal imaging microscope with a green laser (532 nm) as the excitation source, a galvo scanning mirror, an avalanche photodiode for reflectivity measurements (**Figure 5a**), and a current transimpedance amplifier for simultaneous photocurrent measurements as a function of laser position. **Figure 5c** and 5**d** show the photocurrent maps obtained at source-drain voltages of -1 and +1 V, respectively. An asymmetric photocurrent is recorded close to the Cr/Au- $ZrGeTe_4$ contacts which supports the hypothesis that the device is behaving as two opposing photodiodes. An illustrative energy band diagram of the device is shown in **Figure 5b** showing two opposite Schottky barriers. When bias is applied, one Schottky junction is under forward bias and the other is under reverse bias (where the photocurrent is collected). This mechanism has been used to describe the operation of similar van der Waals materials devices, for example those based on InSe, previously.[47] Line-cuts of the photocurrent profile across the device are presented in **Figure 5e**, confirming the asymmetry in photocurrent that one would expect to accompany this mechanism. It can be seen from the current-voltage characteristics of this device (**Figure 5f**) that the open circuit voltage when the laser spot is centered over the left electrode differs from that when the spot is centered over the right electrode (colored dots of **Figure 5a**). The maximum photocurrent for both polarities is similar. These results strongly suggest that majority of photocurrent in these devices is collected by the Schottky barriers, making them photovoltaic detectors, although we note that other mechanisms may provide a non-zero contribution. For example, similar devices with no/small barriers, such as those with $MoO_x$/Au contacts, provided an IR photoresponse, albeit significantly weaker than that measured with Cr/Au contacts. In addition, the small but non-zero response measured whilst the laser is illuminating the contacts suggests the possibility of a contribution from the photothermoelectric effect.[56] Finally, we note that the bias-selectable collection of photocurrent from different regions (i.e. opposite contact regions) demonstrates the potential application of this photodetector as a position sensitive lateral detector.

## Conclusion

In summary, we report the first demonstration of photodetection using $ZrGeTe_4$, which joins a growing family of IR van der Waals materials. In its bulk (multilayer) form, $ZrGeTe_4$ is found to have an indirect bandgap of around ~0.5 eV and is structurally stable under a broad range of conditions up to 140 °C or over ~1 month without encapsulation at room temperature. A simple photodetector structure is demonstrated using symmetrical Cr/Au contacts on a Si/$SiO_2$ substrate, which shows responsivity $R(\lambda)$ values > 0.1 $AW^{-1}$ from visible to short-wave infrared wavelengths ($V_{SD}$ = 1 V, $V_G$ = 0 V). This corresponds to a specific detectivity $D^*$ of ~$10^9$ cm $Hz^{1/2}$ $W^{-1}$ at $\lambda$ = 1.4 μm at room temperature ($V_{SD}$ > ±0.5 V, $V_G$ = 0 V). These values are remarkably high, especially considering the infancy of this material's exploration. The $ZrGeTe_4$ detectors also recorded response times ~50 ns, which is well supported by accompanying 3dB roll-off measurements. LBIC analysis reveals that the device behaves as a set of two opposing photodiodes whereby current can be collected at either side of the device by choosing the $V_{SD}$ bias direction. These results highlight the potential use of $ZrGeTe_4$ in stable, high-performance optoelectronic devices, operating at room temperature.

## Experimental section

### Materials characterization

Zirconium Germanium Telluride ($ZrGeTe_4$) flakes were mechanically exfoliated from a high-quality bulk crystal source (from *2DSemiconductors.com*) and transferred onto Si/$SiO_2$ (285 nm) substrates. X-ray diffraction (XRD) measurements were carried out on a Bruker *D*8 advanced diffractometer equipped with a LynxEye XE detector (1D mode) and Ni-filtered Cu $K\alpha$ radiation source (1.54060 Å) operated at 1600 W. A powder-type XRD geometry (Bragg-Brentano coupled $\theta/2\theta$) was employed with 0.02 degrees and a dwell time of 1 s per step. The sample was rotated during data collection.

Raman spectra were acquired on individual $ZrGeTe_4$ flakes at room temperature with a Renishaw InVia Reflex micro-Raman spectrometer with a 2400 lines/mm grating. The spectrometer was equipped with a green laser (532 nm) that was focused onto the sample with a 100× objective with a numerical aperture NA = 0.95. In-situ annealing up to a temperature of 410 °C in a flowing nitrogen atmosphere was performed with a Linkam stage (THMS600). A long working distance 50× objective was used for the high-temperature measurements. Each spectrum was collected with an acquisition time of 100 s. The laser spot diameter was ~0.9 μm measured via knife edge method. Flakes chosen for the Raman characterization were all of a similar size and thickness to those used for device fabrication.

The thickness of $ZrGeTe_4$ flakes was measured by atomic force microscopy (AFM, MFP-3D from Asylum Research, US) using tapping mode. The AFM image with 256 x 256 pixels was scanned at 0.5 Hz. The cantilever used was Tap 300-G (Budget Sensors) with a spring constant of 40 N/m and a resonance frequency of 300 kHz.

**Device fabrication**

In a manner similar to that employed for the materials characterization samples described above, the ZrGeTe4 devices were assembled on $Si/SiO_2$ (285 nm) substrates by mechanical exfoliation from a high-quality bulk crystal source and dry transfer. Electrical contacts to $ZrGeTe_4$ flakes were patterned via electron-beam lithography (EBL). A 10-nm-thick Cr and 100-nm-thick Au contact stack was deposited by electron-beam evaporation. Following lift-off of Cr/Au in the non-pattered areas, the completed devices were then mounted and wire-bonded into a 28-pin chip carrier for photodetector characterization.

**Device characterization**

The spectral photoresponse of fabricated photodiodes were measured using a custom-built IR characterization platform at the external detector port of a FTIR spectrometer (Perkin Elmer Frontier). The sample interferogram, measured under illumination from a modulated 1,200 K blackbody source, was amplified using a transimpedance amplifier (TIA; SRS 570) and fed back into the FTIR, which performs a Fourier transform to extract a spectrum. The influence of the blackbody's wavelength dependence (as measured using an internal Deuterated triglycine sulfate detector) was corrected in all cases. To accurately measure the responsivity, such as the measurements shown in **Figure 3c**, the set-up was calibrated using a NIST traceable Ge photodiode illuminated under identical conditions. A more detailed explanation of this measurement process is provided elsewhere (see for example the Supporting Information of Ref. 24). Biases were applied using the abovementioned TIA.

The specific detectivity was extracted using the above FTIR responsivity measurements measured at biases of $V_{SD}$= -1.5V, -1.0V, -0.5V, 0V, 0.5V and 1.5V in combination with an estimation of the shot noise from the dark current at the above biases based on the equation $\overline{i_n^2} = 2eI_{dark}\Delta f$. Detectivities at 2.0 and 1.4 um were taken from these calculations to construct Figure 3f.

The visible-NIR photoresponse was measured using a benchtop microscope and lock-in amplifier (SRS830). The sample was illuminated with light from a broadband laser-driven light source

(Energetiq EQ-99x) passed through a monochromator (Princeton Instruments Acton SP2150i) and was mechanically chopped at ~720 Hz. Light was focused onto the device with a 10× 0.17 NA microscope objective (Nikon Plan Fluor). The device was biased at $V_{SD} = 1$ V, and photoresponse amplified with a TIA (SRS 570). The output of the TIA was passed to the lock-in amplifier (SRS SR830), along with the reference signal from the optical chopper. The photocurrent was found from the measured voltage signal by the lock-in amplifier. This process was repeated for a range of wavelengths using the monochromator, in steps of 10 nm. The total optical power was measured using an optical Si power meter (Thorlabs S121C) to calculate the responsivity spectrum in **Figure 3c**.

Linearity measurements were performed using a continuous wave 2.2 μm laser source mechanically chopped at 200 Hz. The detector current in the light/dark was amplified via a TIA (SRS 570) and the resulting voltage difference measured via an oscilloscope, example measurements are shown in **Figure 4a**. The bias for these measurements was applied using the TIA. The illumination intensity was measured for each condition using a NIST traceable Ge photodetector in the same position.

The high frequency response time analysis was performed using a fast 1.55 μm laser diode source (rated to 5 mW, rise/fall times <1 ns) electrically driven by a function generator. The detector current was amplified by a high-speed TIA (Femto DHPCA-100) and measured on an oscilloscope (**Figure 4d**) for rise/fall measurement or fed into a high-speed LIA (SRS844) for 3dB roll-off measurements.

To construct the Tauc plot, reflection and transmission spectra were measured using an FTIR microscope (Perkin Elmer) on individual bulk $ZrGeTe_4$ flakes. During measurements $ZrGeTe_4$ flakes were mounted on high resistivity (> 100 Ωcm) chemically polished silicon wafers, which were measured to have negligible absorption over the region of interest.

Laser beam induced current (LBIC) mapping was performed on a custom-built confocal microscope equipped with a 532-nm laser, high-speed TIA (Femto DLPCA-200) and a galvanometer mirror to scan the laser across the back of a 40× objective. Photocurrent and reflectivity maps were recorded simultaneously. Current-voltage measurements were taken in a two-probe configuration (Keithley 2450).

All measurements above were performed in air environment at room temperature unless otherwise stated.

## Supplementary Material

Raman spectra of $ZrGeTe_4$ before and after phase transformation with a 410 °C anneal (Table S1 and Figure S1), as a function of annealing temperature from 40 ºC to 410 ºC (Figure S2), and as a function of position across the $ZrGeTe_4$ flake surface in the as-exfoliated state (Figure S4). Optical micrograph of a $ZrGeTe_4$ flake as a function of annealing temperature (Figure S3). Source-drain *I-V* curves and transfer curves of representative $ZrGeTe_4$ photodetectors (Figure S5). Bias- and polarisation-dependent photoresponse spectra of $ZrGeTe_4$ devices (Figure S6). Photoresponse of $ZrGeTe_4$ devices over time held in $N_2$ ambient (Figure S7a), and under different gate voltages (Figure S7b). Noise spectral density spectrum (Figure S7c) and detectivities of $ZrGeTe_4$ photodetectors with different device thicknesses (Figure S7d). Impulse response of $ZrGeTe_4$ devices under modulated illumination. (Figure S8).

## Acknowledgement

This work was supported by the Defense Advanced Research Projects Agency (HR0011-16-1-0004) and by the Australian Research Council (DP180104141 & DP210103428). BCJ acknowledges the Australian Research Council Center of Excellence for Quantum Computation and Communication Technology (No. CE170100012). Work was performed in part at the Melbourne Centre for Nanofabrication (MCN) in the Victorian Node of the Australian National Fabrication Facility (ANFF) and at the Melbourne Characterization and Fabrication Platform (MCFP).

## References

1. Mueller, T.; Xia, F.; Avouris, P., Graphene Photodetectors for High-Speed Optical Communications. *Nat. Photon.* **2010,** *4*, 297-301.
2. Barve, A. V.; Lee, S. J.; Noh, S. K.; Krishna, S., Review of Current Progress in Quantum Dot Infrared Photodetectors. *Laser Photonics Rev.* **2010,** *4*, 738-750.
3. Chang, H.-Y.; Yang, S.; Lee, J.; Tao, L.; Hwang, W.-S.; Jena, D.; Lu, N.; Akinwande, D., High-Performance, Highly Bendable Mos2 Transistors with High-K Dielectrics for Flexible Low-Power Systems. *ACS Nano* **2013,** *7*, 5446-5452.
4. Martyniuk, P.; Antoszewski, J.; Martyniuk, M.; Faraone, L.; Rogalski, A., New Concepts in Infrared Photodetector Designs. *Appl. Phys. Lett.* **2014,** *1*, 041102.
5. Ling, X.; Wang, H.; Huang, S.; Xia, F.; Dresselhaus, M. S., The Renaissance of Black Phosphorus. *PNAS* **2015,** *112*, 4523-4530.

6. Bhimanapati, G. R.; Lin, Z.; Meunier, V.; Jung, Y.; Cha, J.; Das, S.; Xiao, D.; Son, Y.; Strano, M. S.; Cooper, V. R.; Liang, L.; Louie, S. G.; Ringe, E.; Zhou, W.; Kim, S. S.; Naik, R. R.; Sumpter, B. G.; Terrones, H.; Xia, F.; Wang, Y.; Zhu, J.; Akinwande, D.; Alem, N.; Schuller, J. A.; Schaak, R. E.; Terrones, M.; Robinson, J. A., Recent Advances in Two-Dimensional Materials Beyond Graphene. *ACS Nano* **2015,** *9*, 11509-11539.

7. Hoang, A. M.; Dehzangi, A.; Adhikary, S.; Razeghi, M., High Performance Bias-Selectable Three-Color Short-Wave/Mid-Wave/Long-Wave Infrared Photodetectors Based on Type-Ii Inas/Gasb/Alsb Superlattices. *Sci. Rep.* **2016,** *6*, 24144.

8. Wang, Q.; Wen, Y.; Cai, K.; Cheng, R.; Yin, L.; Zhang, Y.; Li, J.; Wang, Z.; Wang, F.; Wang, F.; Shifa, T. A.; Jiang, C.; Yang, H.; He, J., Nonvolatile Infrared Memory in Mos2/Pbs Van Der Waals Heterostructures. *Sci. Adv.* **2018,** *4*, eaap7916.

9. Omair, Z.; Scranton, G.; Pazos-Outón, L. M.; Xiao, T. P.; Steiner, M. A.; Ganapati, V.; Peterson, P. F.; Holzrichter, J.; Atwater, H.; Yablonovitch, E., Ultraefficient Thermophotovoltaic Power Conversion by Band-Edge Spectral Filtering. *PNAS* **2019,** *116*, 15356-15361.

10. Guan, X.; Yu, X.; Periyanagounder, D.; Benzigar, M. R.; Huang, J.-K.; Lin, C.-H.; Kim, J.; Singh, S.; Hu, L.; Liu, G.; Li, D.; He, J.-H.; Yan, F.; Wang, Q. J.; Wu, T., Recent Progress in Short- to Long-Wave Infrared Photodetection Using 2d Materials and Heterostructures. *Adv. Opt. Mater.* **2020**, 2001708.

11. Li, N.; Lan, Z.; Lau, Y. S.; Xie, J.; Zhao, D.; Zhu, F., Swir Photodetection and Visualization Realized by Incorporating an Organic Swir Sensitive Bulk Heterojunction. *Adv. Sci.* **2020,** *7*, 2000444.

12. Nishida, K.; Taguchi, K.; Matsumoto, Y., Ingaasp Heterostructure Avalanche Photodiodes with High Avalanche Gain. *Appl. Phys. Lett.* **1979,** *35*, 251-253.

13. Martinelli, R. U.; Zamerowski, T. J.; Longeway, P. A., 2.6 Mm Ingaas Photodiodes. *Appl. Phys. Lett.* **1988,** *53*, 989-991.

14. Rogalski, A.; Adamiec, K.; Rutkowski, J., *Narrow-Gap Semiconductor Photodiodes*. SPIE Press: Washington, 2000; *77*, p 237-375.

15. Rogalski, A., Hgcdte Infrared Detector Material: History, Status and Outlook. *Rep. Prog. Phys.* **2005,** *68*, 2267-2336.

16. Piotrowski, J.; Galus, W.; Grudzien, M., Near Room-Temperature Ir Photo-Detectors. *Infrared Phys.* **1991,** *31*, 1-48.

17. Piotrowski, J.; Rogalski, A., *High-Operating-Temperature Infrared Photodetectors*. SPIE: Bellingham, Washington USA, 2007; p 1-242.

18. Du, S.; Lu, W.; Ali, A.; Zhao, P.; Shehzad, K.; Guo, H.; Ma, L.; Liu, X.; Pi, X.; Wang, P.; Fang, H.; Xu, Z.; Gao, C.; Dan, Y.; Tan, P.; Wang, H.; Lin, C.-T.; Yang, J.; Dong, S.; Cheng, Z.; Li, E.; Yin, W.; Luo, J.; Yu, B.; Hasan, T.; Xu, Y.; Hu, W.; Duan, X., A Broadband Fluorographene Photodetector. *Adv. Mater.* **2017,** *29*, 1700463.

19. Xia, F.; Wang, H.; Jia, Y., Rediscovering Black Phosphorus as an Anisotropic Layered Material for Optoelectronics and Electronics. *Nat. Commun.* **2014,** *5*, 4458.

20. Na, J.; Lee, Y. T.; Lim, J. A.; Hwang, D. K.; Kim, G.-T.; Choi, W. K.; Song, Y.-W., Few-Layer Black Phosphorus Field-Effect Transistors with Reduced Current Fluctuation. *ACS Nano* **2014,** *8*, 11753-11762.

21. Bullock, J.; Amani, M.; Cho, J.; Chen, Y.-Z.; Ahn, G. H.; Adinolfi, V.; Shrestha, V. R.; Gao, Y.; Crozier, K. B.; Chueh, Y.-L.; Javey, A., Polarization-Resolved Black Phosphorus/Molybdenum Disulfide Mid-Wave Infrared Photodiodes with High Detectivity at Room Temperature. *Nat. Photon.* **2018,** *12*, 601-607.

22. Tan, W. C.; Huang, L.; Ng, R. J.; Wang, L.; Hasan, D. M. N.; Duffin, T. J.; Kumar, K. S.; Nijhuis, C. A.; Lee, C.; Ang, K.-W., A Black Phosphorus Carbide Infrared Phototransistor. *Adv. Mater.* **2018,** *30*, 1705039.

23. Azar, N. S.; Bullock, J.; Balendhran, S.; Kim, H.; Javey, A.; Crozier, K. B., Light–Matter Interaction Enhancement in Anisotropic 2d Black Phosphorus Via Polarization-Tailoring Nano-Optics. *ACS Photonics* **2021,** *8*, 1120-1128.

24. Amani, M.; Regan, E.; Bullock, J.; Ahn, G. H.; Javey, A., Mid-Wave Infrared Photoconductors Based on Black Phosphorus-Arsenic Alloys. *ACS Nano* **2017,** *11*, 11724-11731.

25. Yim, C.; Lee, K.; McEvoy, N.; O'Brien, M.; Riazimehr, S.; Berner, N. C.; Cullen, C. P.; Kotakoski, J.; Meyer, J. C.; Lemme, M. C.; Duesberg, G. S., High-Performance Hybrid Electronic Devices from Layered Ptse2 Films Grown at Low Temperature. *ACS Nano* **2016,** *10*, 9550-9558.

26. Yim, C.; McEvoy, N.; Riazimehr, S.; Schneider, D. S.; Gity, F.; Monaghan, S.; Hurley, P. K.; Lemme, M. C.; Duesberg, G. S., Wide Spectral Photoresponse of Layered Platinum Diselenide-Based Photodiodes. *Nano Lett.* **2018,** *18*, 1794-1800.

27. Gong, Y.; Lin, Z.; Chen, Y.-X.; Khan, Q.; Wang, C.; Zhang, B.; Nie, G.; Xie, N.; Li, D., Two-Dimensional Platinum Diselenide: Synthesis, Emerging Applications, and Future Challenges. *Nano-Micro Lett.* **2020,** *12*, 174.

28. Sefidmooye Azar, N.; Bullock, J.; Shrestha, V. R.; Balendhran, S.; Yan, W.; Kim, H.; Javey, A.; Crozier, K. B., Long-Wave Infrared Photodetectors Based on 2d Platinum Diselenide Atop Optical Cavity Substrates. *ACS Nano* **2021,** *15*, 6573-6581.

29. Zeng, L. H.; Wu, D.; Lin, S. H.; Xie, C.; Yuan, H. Y.; Lu, W.; Lau, S. P.; Chai, Y.; Luo, L. B.; Li, Z. J.; Tsang, Y. H., Controlled Synthesis of 2d Palladium Diselenide for Sensitive Photodetector Applications. *Adv. Funct. Mater.* **2019,** *29*, 1806878.

30. Huang, H.; Wang, J.; Hu, W.; Liao, L.; Wang, P.; Wang, X.; Gong, F.; Chen, Y.; Wu, G.; Luo, W.; Shen, H.; Lin, T.; Sun, J.; Meng, X.; Chen, X.; Chu, J., Highly Sensitive Visible to Infrared Mote2photodetectors Enhanced by the Photogating Effect. *Nanotechnology* **2016,** *27*, 445201.

31. Wang, Y.; Wu, P.; Wang, Z.; Luo, M.; Zhong, F.; Ge, X.; Zhang, K.; Peng, M.; Ye, Y.; Li, Q.; Ge, H.; Ye, J.; He, T.; Chen, Y.; Xu, T.; Yu, C.; Wang, Y.; Hu, Z.; Zhou, X.; Shan, C.; Long, M.; Wang, P.; Zhou, P.; Hu, W., Air-Stable Low-Symmetry Narrow-Bandgap 2d Sulfide Niobium for Polarization Photodetection. *Adv. Mater.* **2020,** *32*, 2005037.

32. Amani, M.; Tan, C.; Zhang, G.; Zhao, C.; Bullock, J.; Song, X.; Kim, H.; Shrestha, V. R.; Gao, Y.; Crozier, K. B.; Scott, M.; Javey, A., Solution-Synthesized High-Mobility Tellurium Nanoflakes for Short-Wave Infrared Photodetectors. *ACS Nano* **2018,** *12*, 7253-7263.

33. Peng, M.; Xie, R.; Wang, Z.; Wang, P.; Wang, F.; Ge, H.; Wang, Y.; Zhong, F.; Wu, P.; Ye, J.; Li, Q.; Zhang, L.; Ge, X.; Ye, Y.; Lei, Y.; Jiang, W.; Hu, Z.; Wu, F.; Zhou, X.; Miao, J.; Wang, J.; Yan, H.; Shan, C.; Dai, J.; Chen, C.; Chen, X.; Lu, W.; Hu, W., Blackbody-Sensitive Room-Temperature Infrared Photodetectors Based on Low-Dimensional Tellurium Grown by Chemical Vapor Deposition. *Sci. Adv.* **2021,** *7*, eabf7358.

34. Fitzgerald, E. A.; Xie, Y. H.; Monroe, D.; Silverman, P. J.; Kuo, J. M.; Kortan, A. R.; Thiel, F. A.; Weir, B. E., Relaxed Gexsi1−X Structures for Iii–V Integration with Si and High Mobility Two-Dimensional Electron Gases in Si. *J. Vac. Sci. Technol. B* **1992,** *10*, 1807-1819.

35. Ko, H.; Takei, K.; Kapadia, R.; Chuang, S.; Fang, H.; Leu, P. W.; Ganapathi, K.; Plis, E.; Kim, H. S.; Chen, S.-Y.; Madsen, M.; Ford, A. C.; Chueh, Y.-L.; Krishna, S.; Salahuddin, S.; Javey, A., Ultrathin Compound Semiconductor on Insulator Layers for High-Performance Nanoscale Transistors. *Nature* **2010,** *468*, 286-289.

36. Balendhran, S.; Walia, S.; Nili, H.; Ou, J. Z.; Zhuiykov, S.; Kaner, R. B.; Sriram, S.; Bhaskaran, M.; Kalantar-Zadeh, K., Two-Dimensional Molybdenum Trioxide and Dichalcogenides. *Adv. Funct. Mater.* **2013,** *23*, 3952-3970.

37. Chen, K.; Kapadia, R.; Harker, A.; Desai, S.; Seuk Kang, J.; Chuang, S.; Tosun, M.; Sutter-Fella, C. M.; Tsang, M.; Zeng, Y.; Kiriya, D.; Hazra, J.; Madhvapathy, S. R.; Hettick, M.; Chen, Y.-Z.; Mastandrea, J.; Amani, M.; Cabrini, S.; Chueh, Y.-L.; Ager Iii, J. W.; Chrzan, D. C.; Javey, A., Direct Growth of Single-Crystalline Iii–V Semiconductors on Amorphous Substrates. *Nat. Commun.* **2016,** *7*, 10502.

38. Jiang, T.; Zang, Y.; Sun, H.; Zheng, X.; Liu, Y.; Gong, Y.; Fang, L.; Cheng, X. a.; He, K., Broadband High-Responsivity Photodetectors Based on Large-Scale Topological Crystalline Insulator Snte Ultrathin Film Grown by Molecular Beam Epitaxy. *Adv. Opt. Mater.* **2017,** *5*, 1600727.

39. Kim, Y.; Cruz, S. S.; Lee, K.; Alawode, B. O.; Choi, C.; Song, Y.; Johnson, J. M.; Heidelberger, C.; Kong, W.; Choi, S.; Qiao, K.; Almansouri, I.; Fitzgerald, E. A.; Kong, J.; Kolpak, A. M.; Hwang, J.; Kim, J., Remote Epitaxy through Graphene Enables Two-Dimensional Material-Based Layer Transfer. *Nature* **2017,** *544*, 340-343.

40. Yin, J.; Tan, Z.; Hong, H.; Wu, J.; Yuan, H.; Liu, Y.; Chen, C.; Tan, C.; Yao, F.; Li, T.; Chen, Y.; Liu, Z.; Liu, K.; Peng, H., Ultrafast and Highly Sensitive Infrared Photodetectors Based on Two-Dimensional Oxyselenide Crystals. *Nat. Commun.* **2018,** *9*, 3311.

41. Fang, J.; Zhou, Z.; Xiao, M.; Lou, Z.; Wei, Z.; Shen, G., Recent Advances in Low-Dimensional Semiconductor Nanomaterials and Their Applications in High-Performance Photodetectors. *InfoMat* **2020,** *2*, 291-317.

42. Liu, R.; Wang, F.; Liu, L.; He, X.; Chen, J.; Li, Y.; Zhai, T., Band Alignment Engineering in Two-Dimensional Transition Metal Dichalcogenide-Based Heterostructures for Photodetectors. *Small Structures* **2021,** *2*, 2000136.

43. Gong, W.; Li, L.; Gong, P.; Zhou, Y.; Zhang, Z.; Zhou, W.; Wang, W.; Liu, Z.; Tang, D., Raman Investigation of Layered Zrgete4 Semiconductor. *Appl. Phys. Lett.* **2019,** *114*, 172104.

44. Mar, A.; Ibers, J. A., The Layered Ternary Germanium Tellurides Zrgete4, Hfgete4, and Tigete6: Structure, Bonding, and Physical Properties. *J. Am. Chem. Soc.* **1993,** *115*, 3227-3238.

45. Persson, K., Materials Data on Zrgete4 (Sg:36) by Materials Project. Nov. 2014 ed.; Materials Project: United States, 2014.

46. Das, S.; Chen, H.-Y.; Penumatcha, A. V.; Appenzeller, J., High Performance Multilayer Mos2 Transistors with Scandium Contacts. *Nano Lett.* **2013,** *13*, 100-105.

47. Zhao, Q.; Jie, W.; Wang, T.; Castellanos-Gomez, A.; Frisenda, R., Inse Schottky Diodes Based on Van Der Waals Contacts. *Adv. Funct. Mater.* **2020,** *30*, 2001307.

48. Guo, P.; Liang, J.; Zhou, B.; Wang, W.; Liu, Z., Strong Anisotropy and Layer-Dependent Carrier Mobility of Two-Dimensional Semiconductor Zrgete4. *J. Phys. Condens. Matter* **2020,** *32*, 325502.

49. Coenen, K.; Gallucci, F.; Mezari, B.; Hensen, E.; Van Sint Annaland, M., An in-Situ Ir Study on the Adsorption of Co2 and H2o on Hydrotalcites. *J. CO2 Util.* **2018,** *24*, 228-239.

50. Youngblood, N.; Li, M., Ultrafast Photocurrent Measurements of a Black Phosphorus Photodetector. *Appl. Phys. Lett.* **2017,** *110*, 051102.

51. Tan, C.; Amani, M.; Zhao, C.; Hettick, M.; Song, X.; Lien, D.-H.; Li, H.; Yeh, M.; Shrestha, V. R.; Crozier, K. B.; Scott, M. C.; Javey, A., Evaporated Sexte1-X Thin Films with Tunable Bandgaps for Short-Wave Infrared Photodetectors. *Adv. Mater.* **2020,** *32*, 2001329.

52. Krishnamurthi, V.; Khan, H.; Ahmed, T.; Zavabeti, A.; Tawfik, S. A.; Jain, S. K.; Spencer, M. J. S.; Balendhran, S.; Crozier, K. B.; Li, Z.; Fu, L.; Mohiuddin, M.; Low, M. X.;

Shabbir, B.; Boes, A.; Mitchell, A.; McConville, C. F.; Li, Y.; Kalantar-Zadeh, K.; Mahmood, N.; Walia, S., Liquid-Metal Synthesized Ultrathin Sns Layers for High-Performance Broadband Photodetectors. *Adv. Mater.* **2020,** *32*, 2004247.

53. Vincent, J. D., *Fundamentals of Infrared Detector Operation and Testing*. Wiley: New York, 1990.

54. Piotrowski, J.; Gawron, W., Ultimate Performance of Infrared Photodetectors and Figure of Merit of Detector Material. *Infrared Phys. Techn.* **1997,** *38*, 63-68.

55. Xie, C.; Mak, C.; Tao, X.; Yan, F., Photodetectors Based on Two-Dimensional Layered Materials Beyond Graphene. *Adv. Funct. Mater.* **2017,** *27*, 1603886.

56. Buscema, M.; Barkelid, M.; Zwiller, V.; Van Der Zant, H. S. J.; Steele, G. A.; Castellanos-Gomez, A., Large and Tunable Photothermoelectric Effect in Single-Layer Mos2. *Nano Lett.* **2013,** *13*, 358-363.

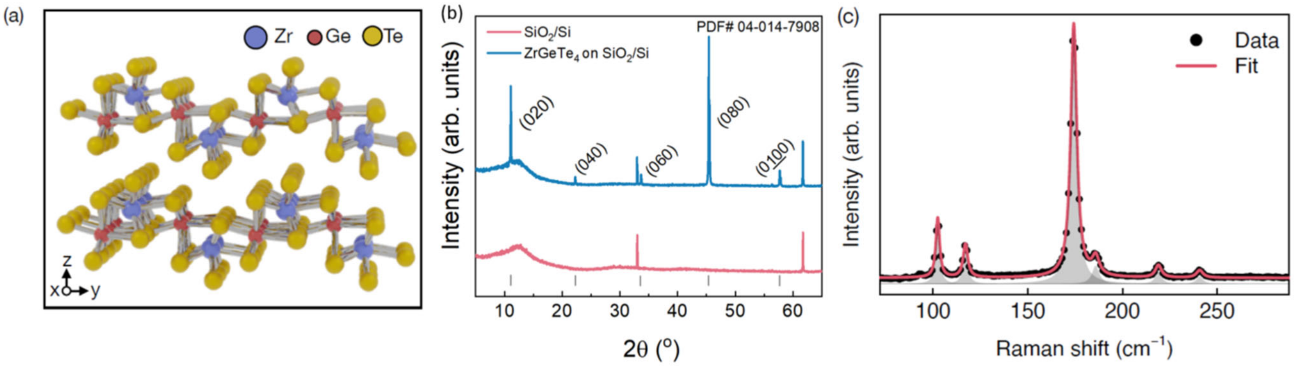

**Figure 1. $ZrGeTe_4$ crystal structure.** **a**, Schematic cross-sectional view of the crystal structure of $ZrGeTe_4$. **b**, XRD of $ZrGeTe_4$ flakes on a $Si/SiO_2$ substrate. The bare substrate is shown for comparison, and the grey vertical lines indicated the expected positions of peaks for Si and $ZrGeTe_4$ ($ZrGeTe_4$ PDF# 04-014-7908). **c**, A representative Raman spectrum of a single flake shortly after exfoliation.

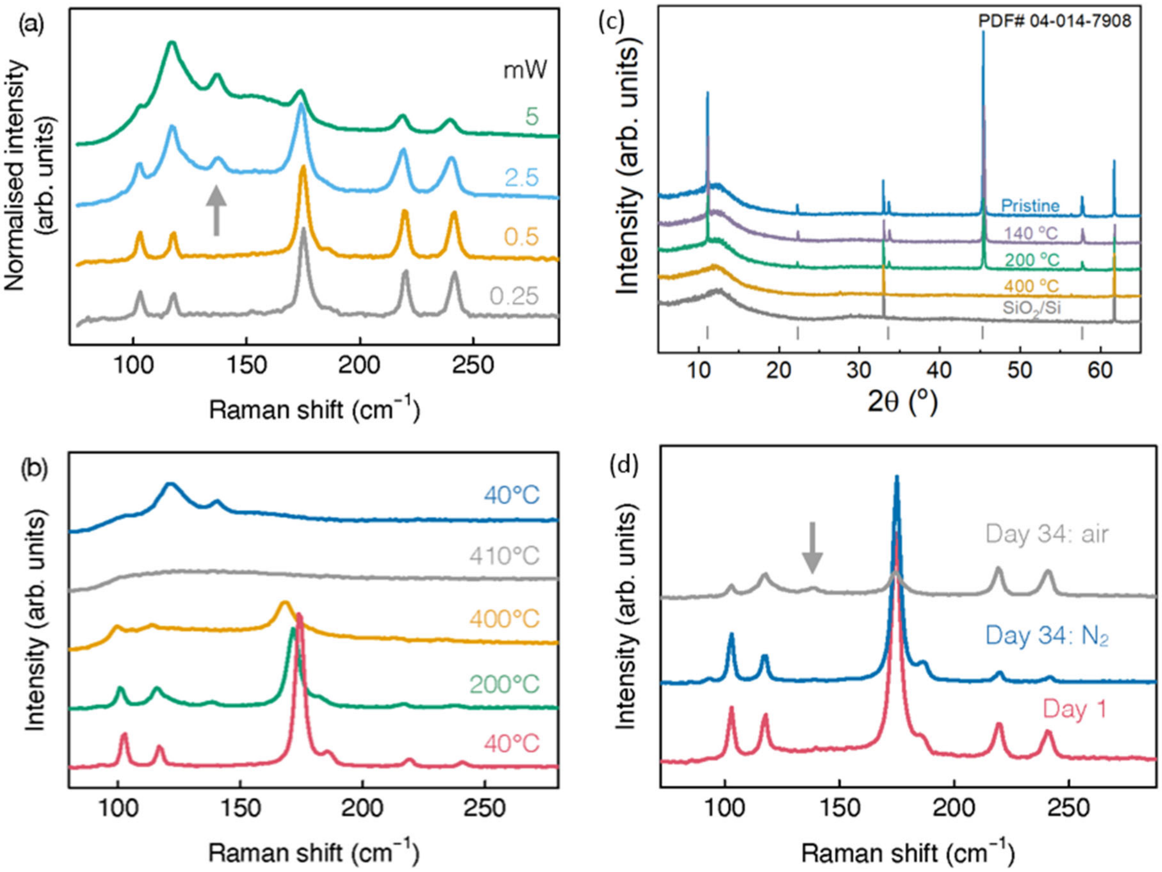

**Figure 2. Environmental stability of $ZrGeTe_4$. a**, Raman spectra under increasing laser ($\lambda = 532$ nm) irradiation power, showing the laser induced material decomposition threshold. 100% laser power density is ~19.3 mW/$\mu m^2$. The arrow indicates a Raman peak associated with the decomposition of $ZrGeTe_4$ as explained in the text. **b**, Raman spectra acquired at various temperatures showing the thermal stability of $ZrGeTe_4$. At ~140 ºC the peak at 140 $cm^{-1}$ becomes apparent. The spectrum at the top is obtained at 40 ºC, after annealing up to 410 °C in $N_2$. **c**, XRD spectra of $ZrGeTe_4$ flakes on $SiO_2$/Si wafer acquired as a function of temperature. The tick marks at the bottom indicate the position of the $ZeGeTe_4$ peaks as shown in Fig. 1b. **d**, Raman spectra of $ZrGeTe_4$ over time held in air and $N_2$ ambient.

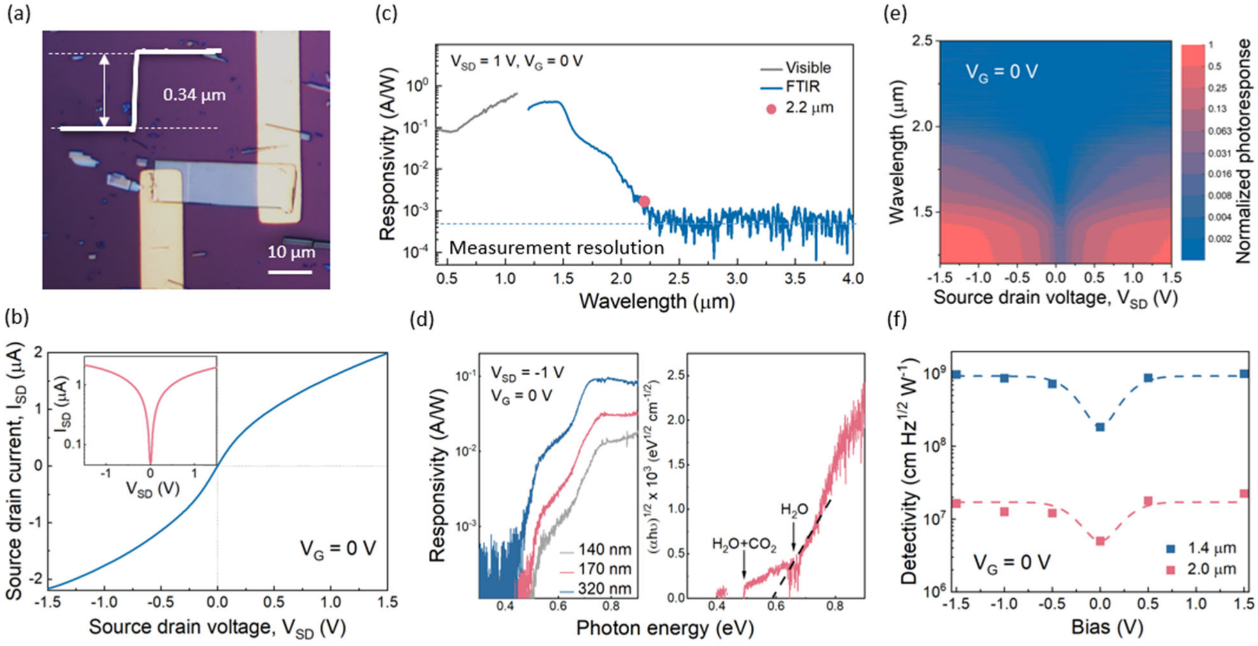

**Figure 3. Photodetector. a**, Optical micrograph of ZrGeTe$_4$ device. Inset: AFM line scan. **b**, Source-drain *I-V* curve of ZrGeTe$_4$ photodetector, measured in dark conditions. Inset: source-drain *I-V* measurement, plotted in log-linear scale. **c**, Responsivity spectrum of ZrGeTe$_4$ device from visible to infrared wavelengths. Pink dot shows responsivity measured with laser (wavelength: 2.2 μm). The resolution for the FTIR measurement conditions is marked by a blue dashed line at around $4\times10^{-3}$ A/W. **d**, Left: zoom in of band edge $R(\lambda)$ for ZrGeTe$_4$ devices of different absorber thickness showing response extending to ~0.5 eV light; right: Tauc plot, which indicates indirect band edge of <0.6 eV for the ZrGeTe$_4$ flake. **e**, Bias dependence map of the spectral photoresponse extrapolated from nine individual photoresponse spectra. **f**, Detectivity of representative ZrGeTe$_4$ device at a wavelength of 1.4 and 2.0 μm vs. source drain bias.

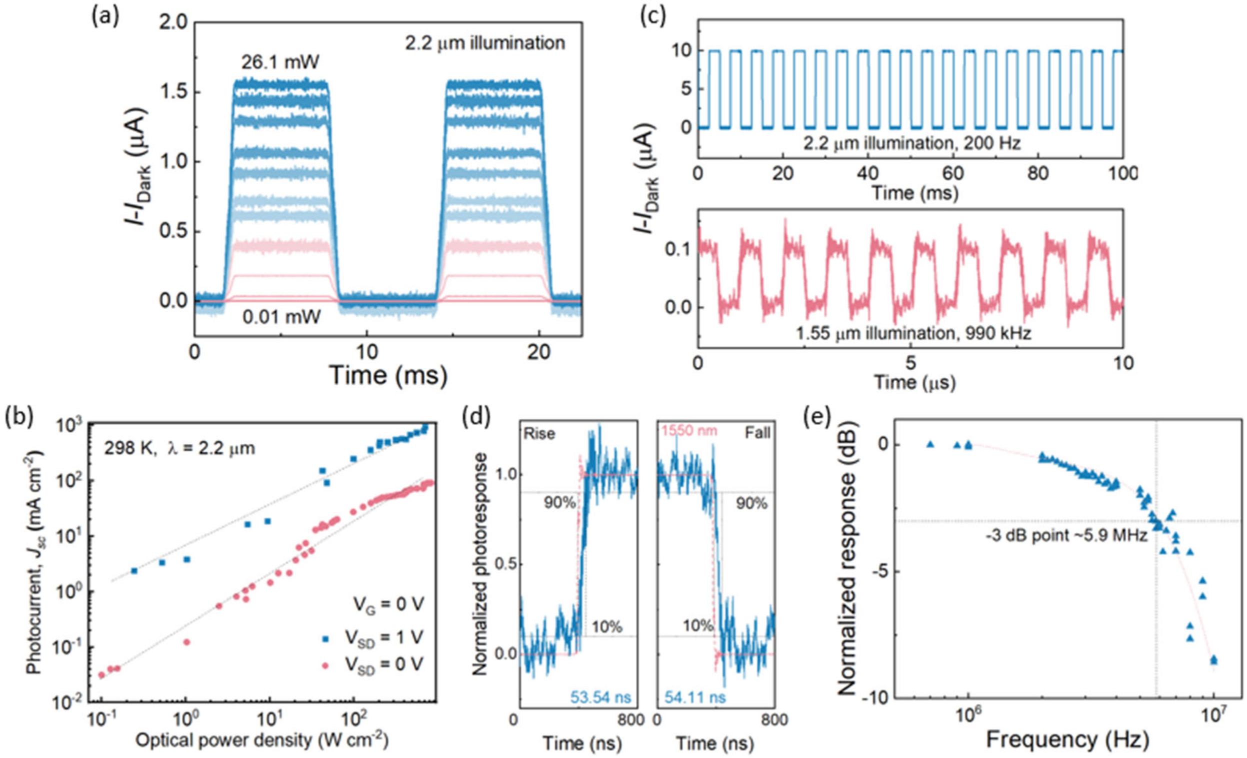

**Figure 4. Linearity and frequency response. a**, Photoresponse of a ZrGeTe$_4$ photodetector at $V_{SD}$=1V under mechanically chopped 2.2 µm illumination at different intensities. **b**, Linearity behaviour of a ZrGeTe$_4$ photodetector under $V_{SD}$= 0 V and 1 V bias, showing consistent proportionality between optical power density and photocurrent density. Excitation is performed with a laser (λ = 2.2 µm) modulated at a frequency of 200 Hz. **c**, Top: Response of ZrGeTe$_4$ under mechanically chopped illumination, showing no observable baseline drift when measuring photoresponse at a fixed incident intensity (λ = 2.2 µm, 200 Hz). Bottom: Response of ZrGeTe$_4$ under high speed electrically modulated illumination again showing no observable baseline drift (λ = 1.55 µm, 990 kHz). **d**, 90%-10% rise and fall times measured under electrically modulated λ = 1.55 µm illumination. Blue solid lines are representative of the ZrGeTe$_4$ photodetector and pink dashed lines show the square wave used to modulate the light source. **e**, change in response amplitude of a ZrGeTe$_4$ photodetector under sinusoidally varying illumination (λ = 1.55 µm), showing a 3-dB roll-off point at a frequency of 5.9 MHz.

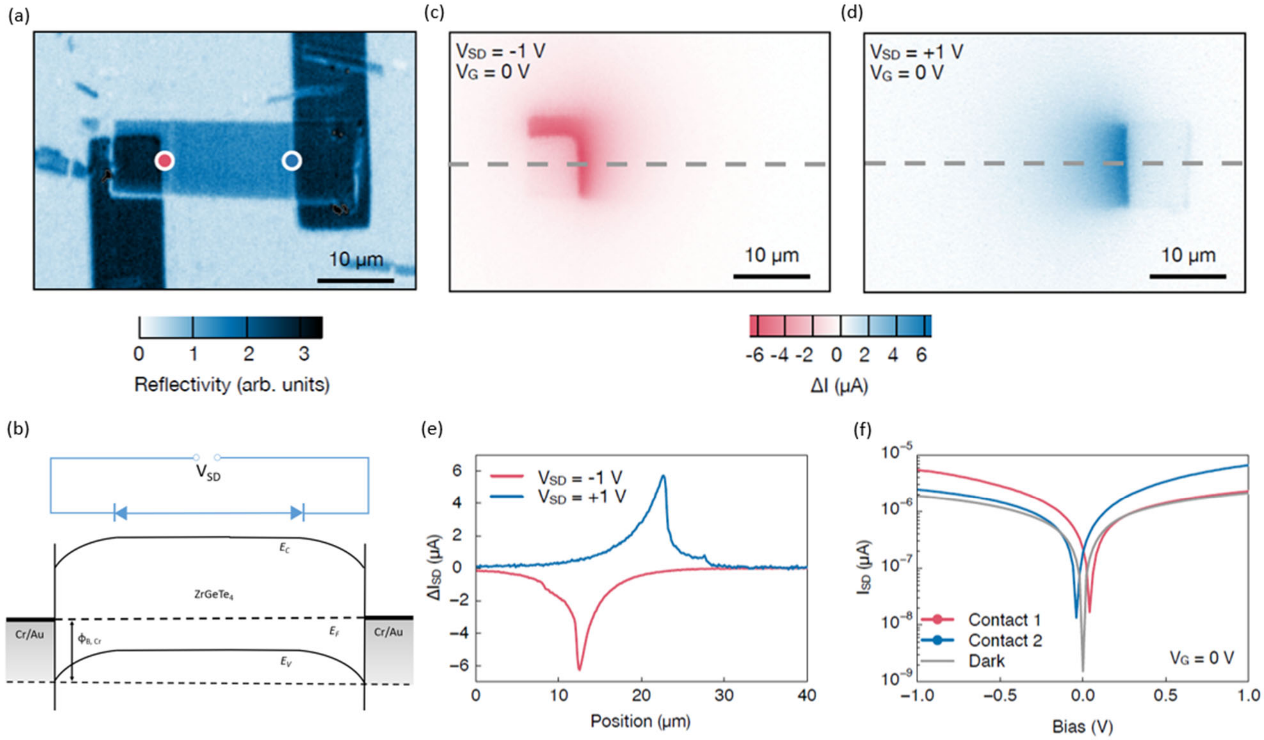

**Figure 5. Laser beam induced current (LBIC) measurement**. **a**, Reflectivity map of ZrGeTe$_4$ device. **b**, Energy band diagram of the contact metal (Cr/Au) and semiconductor (ZrGeTe$_4$). LBIC map of ZrGeTe$_4$ device with the source drain bias at (**c**) -1 V and (**d**) 1 V under laser irradiation. **e**, Line cuts along the dashed line in (**c**) and (**d**). **f**, *I*-*V* curves of the ZrGeTe$_4$ photodetector when the laser is placed at the contacts as indicated in (**a**). The *I*-*V* curve measured in the dark is shown for comparison.

TOC

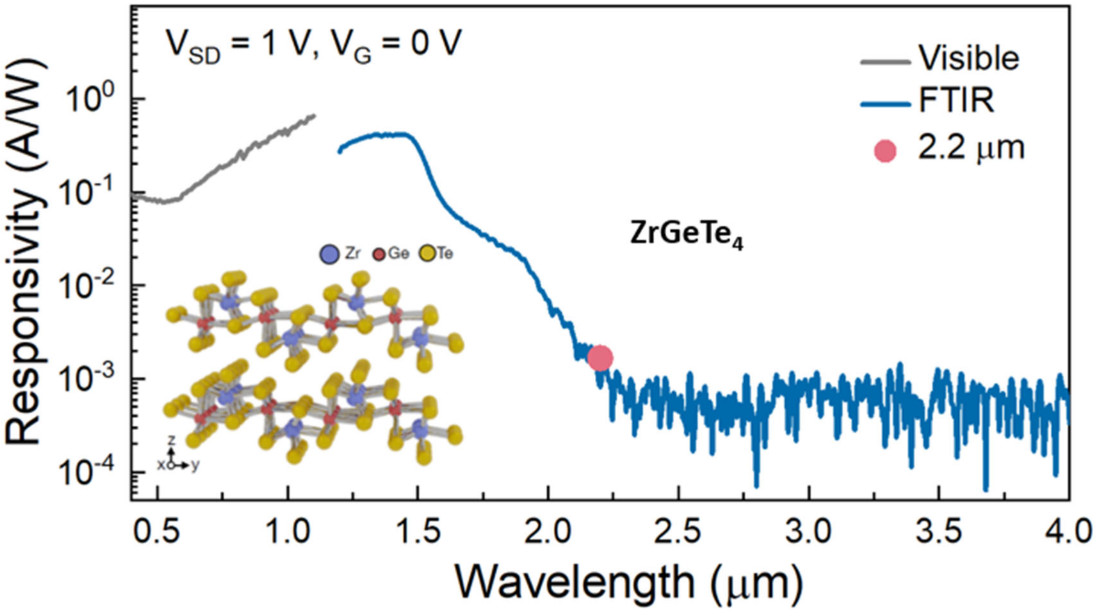
$V_{SD}$ = 1 V, $V_G$ = 0 V
Visible
FTIR
2.2 μm
ZrGeTe$_4$
Zr
Ge
Te
z
x
y
Responsivity (A/W)
$10^0$
$10^{-1}$
$10^{-2}$
$10^{-3}$
$10^{-4}$
Wavelength (μm)
0.5
1.0
1.5
2.0
2.5
3.0
3.5
4.0